LETTERS
https://doi.org/10.1038/s41567-020-1030-6

nature physics

Symmetry breaking in twisted double bilayer graphene

Minhao He[1], Yuhao Li[1], Jiaqi Cai[1], Yang Liu[1], K. Watanabe[2], T. Taniguchi[2], Xiaodong Xu[1,3] ✉ and Matthew Yankowitz[1,3] ✉

The flat bands that appear in some twisted van der Waals heterostructures provide a setting in which strong interactions between electrons lead to a variety of correlated phases[1–20]. In particular, heterostructures of twisted double bilayer graphene host correlated insulating states that can be tuned by both the twist angle and an external electric field[11–14]. Here, we report electrical transport measurements of twisted double bilayer graphene with which we examine the fundamental role of spontaneous symmetry breaking in its phase diagram. The metallic states near each of the correlated insulators exhibit abrupt drops in their resistivity as the temperature is lowered, along with associated nonlinear current–voltage characteristics. Despite qualitative similarities to superconductivity, the simultaneous reversals in the sign of the Hall coefficient point instead to spontaneous symmetry breaking as the origin of the abrupt resistivity drops, whereas Joule heating seems to underlie the nonlinear transport. Our results suggest that similar mechanisms are probably relevant across a broader class of semiconducting flat band van der Waals heterostructures.

Materials with small electronic bandwidths typically manifest effects of electronic correlations at low temperature because of the dominant role of Coulomb interactions between charge carriers. Recently, a new class of correlated materials has arisen in select heterostructures of atomically thin van der Waals crystals with a moiré superlattice, and can be grouped into two categories on the basis of their band structure and crystal symmetry. For example, twisted bilayer graphene (tBLG) consists of two semimetallic monolayer graphene building blocks, and Dirac crossings in tBLG are protected by the product of two-fold rotation and time reversal symmetry (C_2T)[21]. The band structure of tBLG is determined by a complicated interplay of moiré-mediated interlayer tunnelling parameters[22], with flat low-energy bands emerging over an extremely narrow range of twist angles very near 1.1° (refs. [1–10,23–26]). In contrast, all other correlated flat band moiré van der Waals heterostructures investigated so far consist of semiconducting parent crystals—including materials such as WSe_2 and WS_2, which inherently have wide bandgaps[18–20], and materials such as bilayer graphene and ABC trilayer graphene, in which bandgaps can be induced by applying a perpendicular electrical displacement field, D (refs. [11–17,27]). As a consequence, flat bands that can be modified with applied D emerge over a wider range of twist angles in these systems.

Twisted double bilayer graphene (tDBG)—comprising two sheets of Bernal-stacked bilayer graphene rotated by an angle θ—provides a model platform for investigating the properties of a semiconducting flat band moiré van der Waals heterostructure. Previous studies of tDBG have identified a robust correlated insulating (CI) state at half filling of the first moiré conduction band stabilized over a finite range of D, as well as additional CI states at one- and three-quarter fillings that emerge in a magnetic field[11–14]. Abrupt drops in the resistivity of the neighbouring metallic states are observed as the temperature is lowered, saturating to small values at low temperature[11–13].These states also exhibit highly nonlinear current–voltage (I–V) characteristics[12]. Together, these observations raise the possibility that these transport features arise as a consequence of superconductivity[11,12,28]. Although anomalous transport features in the valence band have been reported as well, the role of correlations in these states remains unclear. Overall, transport in tDBG is complicated as it is determined by a number of factors that seem to be of similar magnitude: the width of the flat bands, energy gaps isolating these bands, and the strength of Coulomb interactions. So far, a complete understanding of the correlated phase diagram of tDBG has not been achieved.

Here, we investigate temperature-dependent electrical transport of dual-gated tDBG (Fig. 1a) in five devices with θ ranging from 1.17° to 1.53° (Extended Data Fig. 1). We present data from a device with $\theta = 1.30°$, although we have observed qualitatively similar behaviour in all devices (Extended Data Fig. 2). We first identify transport features corresponding to the single-particle band structure of tDBG by measuring transport at high temperature, such that correlated states are suppressed. Figure 1b shows the device resistivity, ρ, as a function of charge density, n, and D at temperature $T = 30$ K. The top x axis denotes the filling factor of the moiré bands, ν (see Methods). For small $|D| \lesssim 0.3$ V nm^{-1}, the device exhibits only weak resistivity modulations as n and D are tuned. Most notably, a broad cross-like feature is observed for hole-type doping ($\nu < 0$). For larger $|D|$, we observe a substantial difference in ρ between electron- and hole-type doping.

We compare our observations to the single-particle band structure of tDBG, calculated following the procedure developed in ref. [28] with $\theta = 1.30°$. Figure 1c shows the band structure for various values of the interlayer potential, U, and Fig. 1d plots the corresponding density of states as a function of ν and U. The model predicts a semimetal-to-semiconductor transition at the charge neutrality point (CNP; $\nu = 0$) with increasing $|D|$, as well as bandgaps at full filling of the valence and conduction bands ($\nu = \pm 4$, where the factor of 4 accounts for the spin and valley degeneracy of the bands) that diminish with increasing $|D|$. These features correspond well with insulating states observed over similar ranges of $|D|$ in our measurement (Fig. 1b). The model also predicts a bifurcation of the van Hove singularity in the valence band with increasing $|D|$, forming a cross-like feature in the density of states (white contours in Fig. 1d for $\nu < 0$) reminiscent of our observed cross-like

[1]Department of Physics, University of Washington, Seattle, WA, USA. [2]National Institute for Materials Science, Tsukuba, Japan. [3]Department of Materials Science and Engineering, University of Washington, Seattle, WA, USA. ✉e-mail: xuxd@uw.edu; myank@uw.edu

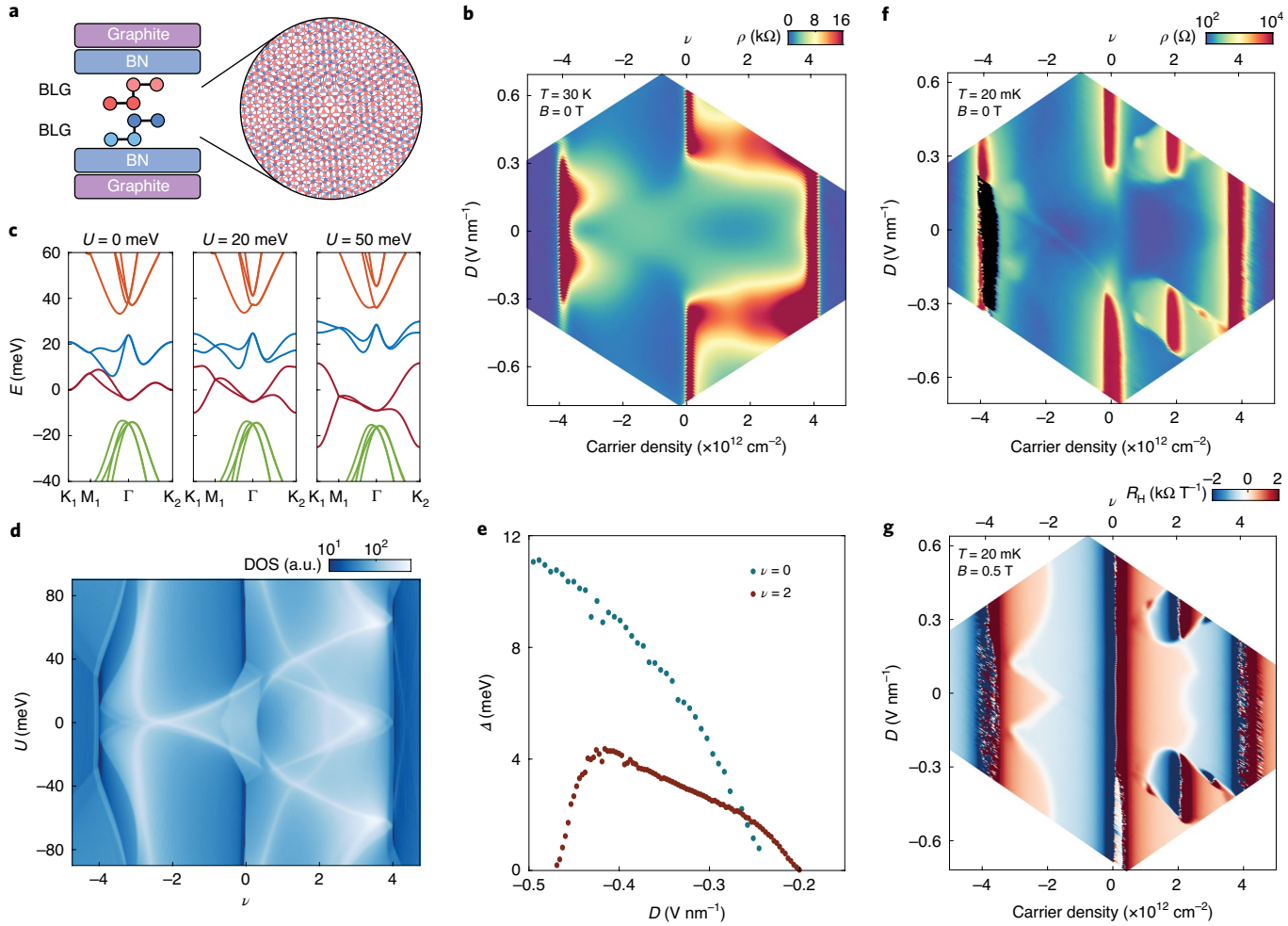

Fig. 1 | Tunable band structure and transport in a 1.30° tDBG device. a, Schematic of a tDBG device encapsulated in hexagonal boron nitride (BN) with graphite gates. **b**, Resistivity of a tDBG device (colour scale) with $\theta = 1.30°$ at $T = 30$ K. The corresponding band filling factor ν is shown on the top x axis. **c**, Calculated band structure of tDBG with $\theta = 1.30°$ at various values of interlayer potential (U). Colouring indicates different moiré subbands. **d**, Calculated density of states (DOS) as a function of ν and U, plotted on a log colour scale. **e**, Energy gaps of the CNP ($\nu = 0$) and the CI state at $\nu = 2$ as a function of D measured by thermal activation. **f**, Resistivity at $T = 20$ mK. The black region corresponds to artificially negative resistance in the contacts used for this measurement. **g**, Hall coefficient (colour scale) antisymmetrized at $|B| = 0.5$ T and $T = 20$ mK.

transport feature in Fig. 1b. Finally, the model predicts that the conduction band flattens with increasing $|D|$, whereas the valence band becomes more dispersive (Fig. 1c). When the two bands are isolated by a gap at the CNP (that is, at large $|D|$), differences in mobility arising from the relative flatness of each band are probably responsible for the large discrepancy in ρ observed between electron- and hole-type doping. Thermal activation measurements at $\nu = 0$ confirm that a gap emerges for $|D| \gtrsim 0.25$ V nm^{-1} and grows monotonically as $|D|$ increases further (Fig. 1e).

We now turn our attention to transport at our base temperature of $T = 20$ mK, shown in Fig. 1f. Most of the transport features described above persist to base temperature, however we observe the emergence of new features in the conduction band at large $|D|$ that are not anticipated within the single-particle model. A well-developed insulating state emerges at half filling of the conduction band ($\nu = 2$) over a finite range of $|D|$, as well as incipient insulating states at $\nu = 1$ and 3. We also observe tilted halo-like features surrounding these states that are characterized by a weak enhancement of ρ. These states arise as a consequence of correlations, as previously identified in prior studies of tDBG[11–14]. Thermal activation measurements of the energy gap of the $\nu = 2$ CI state mark the approximate range of $|D|$ over which correlated states are observed (Fig. 1e). In particular, CI states emerge when $|D|$ is sufficiently large to open a band gap at $\nu = 0$. The suppression of the CI gap at even larger $|D| \approx 0.47$ V nm^{-1} is consistent with previous reports, in which this was argued to be tied to the gap closing at $\nu = 4$ (refs. [11–14]). However, we are not able to directly confirm this in our device owing to limitations in the accessible range of gate voltage.

Corresponding measurements of the Hall coefficient, $R_H = (R_{xy}[B] - R_{xy}[-B])/(2B)$, where B is the magnetic field, provide further insight into the nature of these correlated states (Fig. 1g). The small applied $|B| = 0.5$ T does not substantially alter the transport (Supplementary Fig. 2), and the measurements can therefore be directly compared with Fig. 1f. We observe rapid sign changes in R_H as a function of carrier density at all of the insulating states ($\nu = 0$, 2, 3 and ± 4), as well as a weaker modulation near the incipient CI state at $\nu = 1$, owing to the sign change of the carrier mass on opposite sides of the bandgaps. R_H also changes sign at partial band filling in regions of the phase diagram that are well described by single-particle considerations, consistent with the required reversal of the carrier sign as the band is tuned from empty to filled. We observe additional sign changes in R_H that correspond nearly

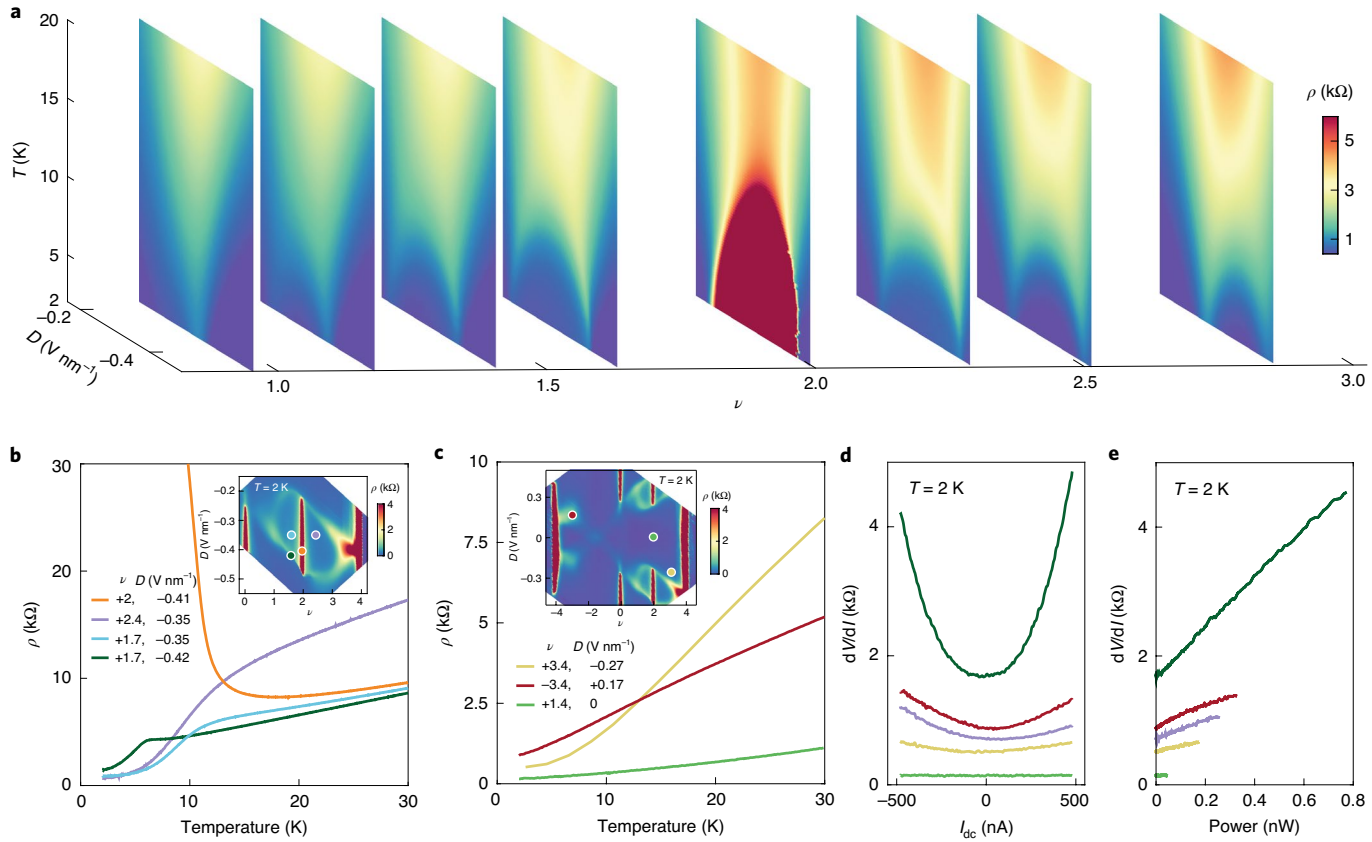

Fig. 2 | Temperature-dependent transport and Joule heating in tDBG. a, Resistivity as a function of temperature and displacement field at a few select values of ν. **b**,**c**, $\rho(T)$ inside (**b**) and outside (**c**) the halo region at select values of (ν, D) denoted by the colour-coded circle markers in the insets. Insets show resistivity maps at $T = 2$ K. **d**, Differential resistance versus applied d.c. current bias at $T = 2$ K for a representative subset of the curves in **b** and **c** (see the respective legends). **e**, Differential resistance as a function of the calculated Joule heating power ($P = IV$). The curves are an average of the positive and negative values of I_{dc} in **d**.

exactly to the boundary of the halo observed in measurements of ρ in Fig. 1f. Furthermore, replica halo features are also apparent in R_H surrounding $\nu = 1$ and 3. As we will discuss in detail later, these sign reversals arise as a consequence of correlations restructuring the bands.

We investigate the properties of the metallic states by measuring the temperature dependence of ρ. Figure 2a shows $\rho(T)$ as a function of D for a few select values of ν. The development of the CI state at $\nu = 2$ results in an arch-like feature centred at optimal D, with an associated metal–insulator transition at $T \approx 15$ K. The arch-like feature persists for $\nu \neq 2$; however, in contrast, ρ continues to decrease monotonically as the temperature is lowered. The maximum onset temperature of the arch decreases as ν is detuned further from 2, with the arms of the arches at base temperature corresponding to the boundaries of the primary halo in Fig. 1f,g.

Figure 2b shows $\rho(T)$ at four values of (ν, D) within the halo, as denoted in the inset. The orange curve exhibits a metal–insulator transition associated with the development of the CI state at $\nu = 2$. Away from $\nu = 2$, $\rho(T)$ scales linearly with T at high temperatures, but further exhibits an abrupt drop at a temperature corresponding to the formation of the arch in Fig. 2a, before eventually beginning to saturate to a finite residual resistivity at low T. The dark green curve, acquired precisely on the halo boundary, exhibits the most rapid drop in $\rho(T)$. In contrast, transport outside the halo region does not manifest such resistivity drops, instead it exhibits linear-in-T resistivity until eventually saturating to a finite residual resistivity at low T (Fig. 2c). Such behaviour is commonly observed in graphene[29,30], and here we observe a very large slope of a few hundred ohms per Kelvin, comparable to previous observations in tBLG[5,6].

The abrupt drops in $\rho(T)$ in curves acquired within the halo region resemble the onset of superconductivity. However, despite heavy electronic filtering, we observe a finite residual resistivity at base temperature of a few hundred ohms in all devices. As an additional check, we measure the differential resistance, dV/dI, as a function of applied d.c. current bias, I_{dc} at $T = 2$ K (Fig. 2d). The curves are acquired at the same (ν, D) as those in Fig. 2b,c. Inside the halo (dark green and purple curves), we observe nonlinear transport that is not generally anticipated for a typical metal. Although superconducting states also exhibit nonlinear I–V, we do not observe signatures of a well-defined critical current in our measurements, nor do we observe saturation to a 'normal state' value of dV/dI up to $I_{dc} = 500$ nA. Furthermore, nonlinear transport is not limited solely to curves acquired within the halo, but is also observed outside the halo in cases where the corresponding $\rho(T)$ does not exhibit an abrupt drop (yellow and red curves). Figure 2e shows dV/dI as a function of the dissipated power $P = IV$. In general, larger nonlinearities in I–V correspond to higher power dissipation, pointing to Joule heating as the most likely underlying mechanism. The dV/dI acquired on the boundary of the halo is the most strongly nonlinear (dark green curve), consistent with a substantial contribution from the large increase in $\rho(T)$ at low T (Fig. 2b). In contrast, transport is linear in the light green curve, which exhibits the lowest ρ at all T. Overall, nonlinear transport in our devices is generically observed in states with large residual resistivity at base temperature

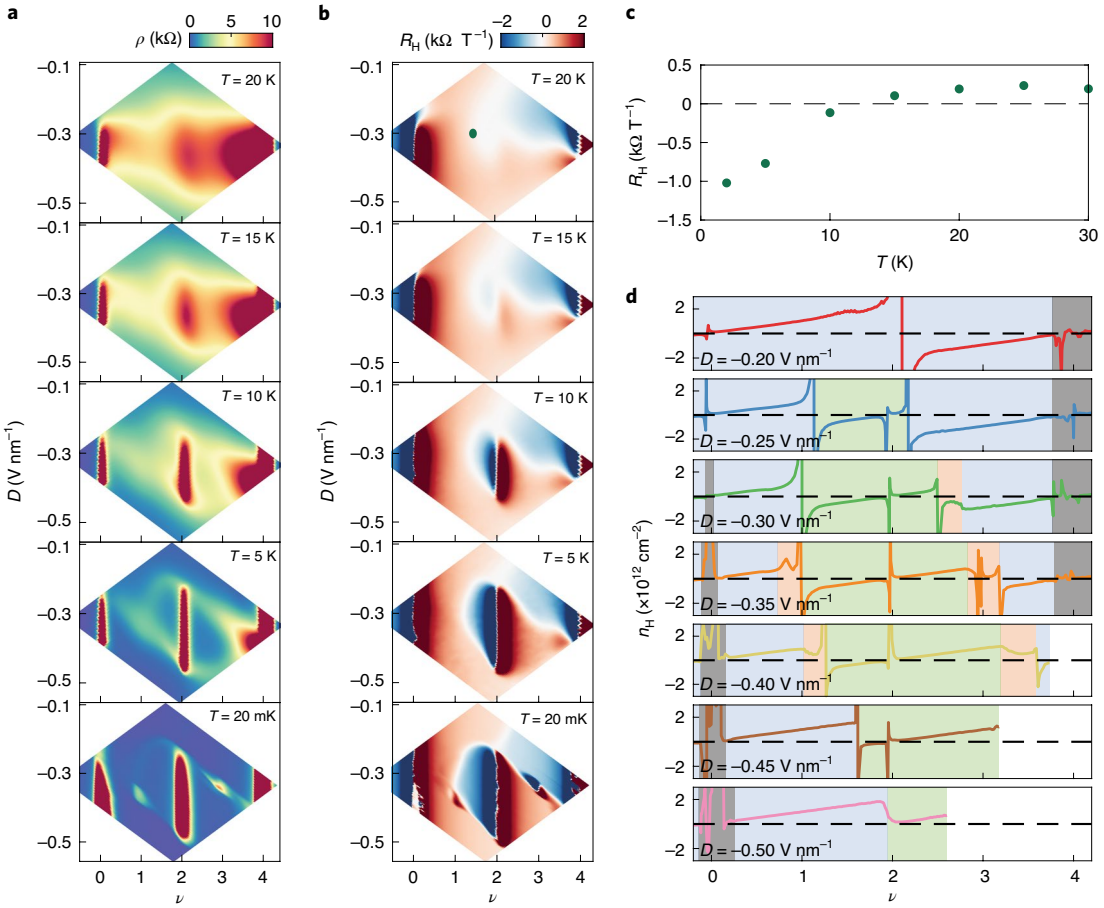

Fig. 3 | Evidence for spontaneous symmetry breaking inside the halo region. a, Resistivity acquired at $T = 20$ K, 15 K, 10 K, 5 K and 20 mK (top to bottom). **b**, Corresponding maps of R_H. **c**, R_H as a function of T acquired at slight underdoping of the CI state at $\nu = 2$ (corresponding to the green circle marker in the top map in **b**). **d**, Hall density as a function of ν at various values of D. The colour shading denotes regions of the phase diagram with different inferred degeneracy: blue corresponds to four-fold degeneracy, green corresponds to two-fold degeneracy and orange has no remaining degeneracy. Grey regions denote insulating states at $\nu = 0$ and 4.

and large $d\rho/dT$, and therefore does not seem to be a signature of superconductivity.

Figure 3a,b shows maps of ρ and R_H, respectively, surrounding the halo region from $T = 20$ mK to 20 K acquired in approximately 5 K steps. The CI state and the surrounding resistive halo smear together as the temperature is raised (Fig. 3a), eventually forming a highly resistive stripe spanning the entire conduction band. In the corresponding R_H map (Fig. 3b), the $R_H = 0$ contour shrinks towards $\nu = 2$ as the temperature is raised. This is particularly evident for $\nu < 2$, as the corresponding contour for $\nu > 2$ is complicated by thermal activation to the higher-energy remote band[6]. Within much of the halo region, we find that the sign of R_H reverses as the temperature is lowered (Fig. 3c, corresponding to the green circle in Fig. 3b).

Given the apparent association of the halo features in ρ with the sign changes in the Hall density n_H, we interpret the halo regions as footprints of spontaneous symmetry breaking within the phase diagram of tDBG. Figure 3d shows the corresponding evolution of the Hall density, $n_H = 1/eR_H$, for select values of D at $T = 20$ mK. Whereas n_H exhibits a single sign change near $\nu = 2$ at small D, the emergence of the CI states results in additional sign changes and abrupt resets of n_H at integer ν. The sign of n_H follows single-particle expectations within the blue shaded regions of Fig. 3d. We therefore infer that these regions correspond to metallic states with full spin and valley degeneracy. The green shading corresponds to the primary halo region observed in Fig. 3a,b, and is bounded by additional sign changes in n_H. This denotes regions of the phase diagram associated with the formation of the CI state at $\nu = 2$, in which we presume that a single degeneracy is lifted. The orange shading corresponds to the replica halos in Fig. 3a,b, and is bounded by additional abrupt resets in n_H. This marks regions of the phase diagram that we presume to have no remaining degeneracies owing to the additional development of the CI states at $\nu = 1$ and 3.

Collectively, our results suggest that correlations dramatically restructure the Fermi surface as a function of n, D and T. In particular, correlated states emerge as T is lowered, and seem to be strongest at optimal values of $\nu \approx 2$ and $D \approx 0.35$ V nm^{-1} at this twist angle. At base temperature, detuning n and D from these values further modifies the band structure and results in the formation of additional correlated ground states. Within the halo region, abrupt drops in $\rho(T)$ arise concomitantly with sign changes in R_H, and therefore seem to be directly associated with the development of symmetry-broken states within the isolated flat band.

Our measurements of the energy gap of the $\nu = 2$ CI state do not scale trivially with in-plane magnetic field (see Supplementary Section 2 and Supplementary Fig. 6), possibly due to a unique orbital contribution in tDBG[28] that arises in addition to the usual Zeeman energy. Although we are not able to unambiguously determine the ground state ordering of the CI states or the neighbouring symmetry-broken metallic states, the CI states always become more resistive with in-plane field, suggestive of spin-polarized ordering.

The precise mechanism driving the abrupt drop in $\rho(T)$ within the halo region in tDBG remains an open question, however, qualitatively similar transport has previously been observed in certain bulk crystals owing to reduced scattering associated with the emergence of various types of magnetic ordering[31], including in MnSi (ref. [32]) and $BaFe_2As_2$ (ref. [33]). Although we do not observe any signatures of an anomalous Hall effect within the halo region (Supplementary Fig. S3), numerous magnetically ordered ground states with zero net Berry curvature remain possible even in its absence. The abrupt reduction in ρ may also be associated with reduced inelastic scattering in the symmetry-broken band or from variations in the strength of electron–phonon coupling. Further theoretical analysis is necessary to provide a detailed quantitative understanding of these observations.

Finally, it is interesting to consider our results in the context of other semiconducting flat band moiré van der Waals heterostructures. Recent studies of twisted WSe_2 (ref. [20]) and ABC trilayer graphene aligned with hexagonal boron nitride[16] have also reported displacement field-tunable CI states emerging at integer ν, along with associated reversals in the sign of n_H on either side of the CI states. Similar to tDBG, CI states emerge in trilayer graphene only at large $|D|$, when a gap at the CNP isolates the bands. When the combination of (ν, D) is detuned slightly from the CI states, abrupt drops in $\rho(T)$ and associated nonlinear I–V suggestive of superconductivity are also observed[16,20]. Often, the residual resistivity at base temperature is not precisely zero[16]. Many of these observations contrast with tBLG, in which unambiguous signatures of superconductivity are routinely observed (see Methods). Although direct comparisons are difficult, the qualitative similarities of our results with the other semiconducting flat band systems studied so far motivates the possibility that in all such cases, the nonlinear I–V may be governed by Joule heating and the abrupt resistivity drops may result from spontaneous symmetry breaking.

Online content

Any methods, additional references, Nature Research reporting summaries, source data, extended data, supplementary information, acknowledgements, peer review information; details of author contributions and competing interests; and statements of data and code availability are available at https://doi.org/10.1038/s41567-020-1030-6.

Received: 20 February 2020; Accepted: 3 July 2020;
Published online: 14 September 2020

References

1. Cao, Y. et al. Correlated insulator behaviour at half-filling in magic-angle graphene superlattices. *Nature* **556**, 80–84 (2018).
2. Cao, Y. et al. Unconventional superconductivity in magic-angle graphene superlattices. *Nature* **556**, 43–50 (2018).
3. Yankowitz, M. et al. Tuning superconductivity in twisted bilayer graphene. *Science* **363**, 1059–1064 (2019).
4. Sharpe, A. L. et al. Emergent ferromagnetism near three-quarters filling in twisted bilayer graphene. *Science* **365**, 605–608 (2019).
5. Cao, Y. et al. Strange metal in magic-angle graphene with near Planckian dissipation. *Phys. Rev. Lett.* **124**, 076801 (2020).
6. Polshyn, H. et al. Large linear-in-temperature resistivity in twisted bilayer graphene. *Nat. Phys.* **15**, 1011–1016 (2019).
7. Lu, X. et al. Superconductors, orbital magnets, and correlated states in magic angle bilayer graphene. *Nature* **574**, 653–657 (2019).
8. Serlin, M. et al. Intrinsic quantized anomalous Hall effect in a moiré heterostructure. *Science* **367**, 900–903 (2020).
9. Stepanov, P. et al. Untying the insulating and superconducting orders in magic-angle graphene. *Nature* **583**, 375–378 (2020).
10. Saito, Y., Ge, J., Watanabe, K., Tanighuchi, T. & Young, A. F. Independent superconductors and correlated insulators in twisted bilayer graphene. *Nat. Phys.* https://doi.org/10.1038/s41567-020-0928-3 (2020).
11. Shen, C. et al. Correlated states in twisted double bilayer graphene. *Nat. Phys.* **16**, 520–525 (2020).
12. Liu, X. et al. Tunable spin-polarized correlated states in twisted double bilayer graphene. *Nature* **583**, 221–225 (2020).
13. Cao, Y. et al. Tunable correlated states and spin-polarized phases in twisted bilayer-bilayer graphene. *Nature* **583**, 215–220 (2020).
14. Burg, G. W. et al. Correlated insulating states in twisted double bilayer graphene. *Phys. Rev. Lett.* **123**, 197702 (2019).
15. Chen, G. et al. Evidence of a gate-tunable Mott insulator in a trilayer graphene moiré superlattice. *Nat. Phys.* **15**, 237–241 (2019).
16. Chen, G. et al. Signatures of tunable superconductivity in a trilayer graphene moiré superlattice. *Nature* **572**, 215–219 (2019).
17. Chen, G. et al. Tunable correlated Chern insulator and ferromagnetism in a moiré superlattice. *Nature* **579**, 56–61 (2020).
18. Tang, Y. et al. Simulation of Hubbard model physics in WSe_2/WS_2 moiré superlattices. *Nature* **579**, 353–358 (2020).
19. Regan, E. C. et al. Mott and generalized wigner crystal states in WSe_2/WS_2 moiré superlattices. *Nature* **579**, 359–363 (2020).
20. Wang, L. et al. Correlated electronic phases in twisted bilayer transistion metal dichalcogenides. *Nat. Mater.* **19**, 861–866 (2020).
21. Po, H. C., Zou, L., Vishwanath, A. & Senthil, T. Origin of Mott insulating behavior and superconductivity in twisted bilayer graphene. *Phys. Rev. X* **8**, 031089 (2018).
22. Bistritzer, R. & MacDonald, A. H. Moiré bands in twisted double-layer graphene. *Proc. Natl Acad. Sci. USA* **108**, 12233–12237 (2011).
23. Jiang, Y. et al. Charge order and broken rotational symmetry in magic-angle twisted bilayer graphene. *Nature* **573**, 91–95 (2019).
24. Kerelsky, A. et al. Maximized electron interactions at the magic angle in twisted bilayer graphene. *Nature* **572**, 95–100 (2019).
25. Xie, Y. et al. Spectroscopic signatures of many-body correlations in magic-angle twisted bilayer graphene. *Nature* **572**, 101–105 (2019).
26. Choi, Y. et al. Electronic correlations in twisted bilayer graphene near the magic angle. *Nat. Phys.* **15**, 1174–1180 (2019).
27. Adak, P. C. et al. Tunable bandwidths and gaps in twisted double bilayer graphene on the verge of correlations. *Phys. Rev. B* **101**, 125428 (2020).
28. Lee, J. Y. et al. Theory of correlated insulating behaviour and spin-triplet superconductivity in twisted double bilayer graphene. *Nat. Commun.* **10**, 5333 (2019).
29. Chen, J.-H., Jang, C., Xiao, S., Ishigami, M. & Fuhrer, M. S. Intrinsic and extrinsic performance limits of graphene devices on SiO_2. *Nat. Nanotechnol.* **3**, 206–209 (2008).
30. Dean, C. R. et al. Boron nitride substrates for high-quality graphene electronics. *Nat. Nanotechnol.* **5**, 722–726 (2010).
31. Kasuya, T. Electrical resistance of ferromagnetic metals. *Prog. Theor. Phys.* **16**, 58–63 (1956).
32. Petrova, A. E., Bauer, E. D., Krasnorussky, V. & Stishov, S. M. Behavior of the electrical resistivity of MnSi at the ferromagnetic phase transition. *Phys. Rev. B* **74**, 092401 (2006).
33. Rotter, M. et al. Spin-density-wave anomaly at 140 K in the ternary iron arsenide $BaFe_2As_2$. *Phys. Rev. B* **78**, 020503(R) (2008).

Methods

Device fabrication. tDBG devices are fabricated using the tear-and-stack method[34,35], or by first cutting the bilayer graphene using an atomic force microscope tip to mitigate strain in the heterostructure[10,15]. tDBG is encapsulated between flakes of hexagonal boron nitride (BN) with typical thickness of 30–50 nm. The devices feature graphite top and bottom gates with typical flake thicknesses around 5 nm. Heterostructures of graphite/BN/tDBG/BN/graphite are assembled using standard dry-transfer techniques with a polycarbonate film on top of a polydimethyl siloxane stamp[36]. Completed heterostructures are transferred onto a Si/SiO_2 wafer. Conventional plasma etching and metal deposition techniques are used to fabricate samples into Hall bar geometries[36].

Transport measurements. Transport measurements are conducted in a four-terminal geometry with typical a.c. current excitations of 5–10 nA using a standard lock-in technique at 13.3 Hz. Regions of the tDBG extend beyond both the graphite top and bottom gates, and in some measurements are doped by applying a voltage to the Si gate. Transport characterization at temperatures above 2 K was performed in a PPMS DynaCool. Transport characterization down to 20 mK was performed in a Bluefors dilution refrigerator with low-temperature electronic filtering. The dual-gated geometry of the devices allows independent tuning of n and D. We calculate $n=(V_tC_t+V_bC_b)/e$, and $D=(V_tC_t-V_bC_b)/2\epsilon_0$, where C_t and C_b are the top and bottom gate capacitances, V_t and V_b are the top and bottom gate voltages, e is the electron charge and ϵ_0 is the vacuum permittivity.

Twist angle determination. The twist angle θ is determined from the values of n at which the insulating states at full band filling ($\nu=\pm4$) appear, following $n=8\theta^2/\sqrt{3}a^2$, where $a=0.246$ nm is the lattice constant of graphene. The filling factor is defined as $\nu=\sqrt{3}\lambda^2 n/2$, where λ is the period of the moiré. The charge carrier density corresponding to $\nu=\pm4$ is determined by tracing the sequence of quantum oscillations in a magnetic field projecting to full band filling at $B=0$.

Band structure calculation. The band structure of tDBG is calculated using a generalization of Bistritzer–MacDonald model[22]. The effect of the moiré potential is captured by a tight-binding model in an effective K space honeycomb lattice following the details of ref. [28], in which the effects of lattice relaxations are captured phenomenologically by tuning the hopping parameters.

Transport in additional devices. We investigate transport in a total of five tDBG devices with different twist angles, $\theta=1.17°$, 1.25°, 1.30°, 1.35° and 1.53° (devices D1, D2, D3, D4 and D5, respectively). Device D3 is discussed extensively in the main text. Extended Data Fig. 1 shows optical microscope images of all five devices. Extended Data Fig. 2a–j shows maps of ρ and R_H as a function of n and D for each device. All measurements are acquired at $T=2$ K, except for device D3 in which $T=20$ mK. We observe qualitatively similar transport features across all five devices, including a semimetal-to-semiconductor transition at $\nu=0$ with increasing $|D|$, insulating states at $\nu=\pm4$, a cross-like feature for $\nu<0$ and insulating or resistive states at $\nu=2$ surrounded by halo features over a finite range of $|D|$. Insulating states at $\nu=\pm4$ exist over a smaller range of $|D|$ for smaller twist angles, consistent with tight-binding model calculations and with previous experimental reports[11–14,28]. The CI states at $\nu=2$ are strongest in devices D2, D3 and D4, weaker in device D1, and barely developed in device D5. In the absence of a magnetic field, incipient CI states at $\nu=1$ and 3 are only observed in device D3 (Extended Data Fig. 3), however the base temperature for all other devices was limited to 2 K.

Extended Data Fig. 2k–o shows corresponding phase diagrams for $\nu>0$ as a function of D. The phase diagrams are shown for $D<0$, but are approximately equivalent for $D>0$ within our experimental resolution. The colour shading denotes regions of the phase diagram with different inferred degeneracy, where blue corresponds to four-fold degeneracy, green corresponds to two-fold degeneracy and orange has no remaining degeneracy (consistent with the colours used in Fig. 3d). The dark grey lines denote CI states. The light grey corresponds to regions of the phase diagram that are experimentally inaccessible owing to the onset of dielectric breakdown to the gates. The boundaries of the symmetry-broken regions of the phase diagram correspond to regions of the R_H map in which the sign inverts or there is an abrupt change in magnitude. The symmetry-broken region of the phase diagram seems to be largest around $\theta=1.30°$, and shrinks for both larger and smaller twist angles. Correlated states at one-quarter band filling also emerge only near this twist angle. In devices D1 and D5, we observe large regions of metallic symmetry-broken states even in the absence of a well-developed CI state at $\nu=$, suggesting that the bands have started to split but are not yet fully gapped.

Abrupt drops in $\rho(T)$ are observed within the halo regions of D1, D2 and D3 (comparable temperature dependence was not acquired in D4 and D5). In addition to the data in Fig. 2b, Extended Data Fig. 4 shows $\rho(T)$ for devices D1 and D2. The similarity of the transport within the halo regions across multiple devices further confirms our interpretation that the observed correlated phase diagram arises as a consequence of spontaneous symmetry breaking.

Transport in a parallel magnetic field. Extended Data Fig. 5 shows maps of ρ and R_{xy} for devices D2 and D3 with an in-plane magnetic field $B_{\parallel}=9$ T, acquired at $T=2$ K. The R_{xy} maps are antisymmetrized via the addition of a small (<0.5 T) out-of-plane field component. CI states at $\nu=1$, 2 and 3 are observed in both devices. Similar to the case of $B=0$ T, we observe sign changes in R_{xy} associated with the formation of each of these states, corresponding approximately to the halo regions in ρ. We also observe a splitting of the cross-like features for electron-type doping ($\nu<0$). We attribute this effect to a Zeeman splitting of the van Hove singularities in the valence band.

Comparison with tBLG. Our observations in tDBG contrast previous results in tBLG in a number of ways. First, tBLG exhibits numerous clear signatures of superconductivity: rapid drops to immeasurably small ρ below a critical temperature, well-defined critical currents in I–V measurements and signatures of Fraunhofer-like phase coherent transport in a magnetic field owing to sample inhomogeneity[2,3]. Second, recent local spectroscopy measurements in tBLG have revealed a cascade sequence of abrupt symmetry breakings in which the initial four-fold degeneracy of each flat band is reduced by one each time the chemical potential crosses integer ν (refs. [37,38]). Correspondingly, transport measurements exhibit abrupt resets of n_H to zero only on overdoping of a well-developed CI state, and generally do not come with an associated sign change[2,3,7,9,10]. This behaviour contrasts our observations in tDBG and previous observations in other semiconducting flat band systems, where the sign of n_H reverses and a symmetry is broken even when the chemical potential is at substantial underdoping of a CI state (Fig. 3d). Notably, similar sign changes in n_H are also observed surrounding $\nu=2$ in tBLG aligned with BN[8], in which C_2 rotation symmetry is broken and a single-particle gap opens at $\nu=0$. Together, this may point to the critical role of C_2T symmetry in determining the correlated phase diagram of flat band moiré van der Waals heterostructures, however, additional experimental and theoretical effort will be necessary to adequately address this point.

Data availability

Source data are available for this paper. All other data that support the plots within this paper and other findings of this study are available from the corresponding authors on reasonable request.

References

34. Kim, K. et al. van der Waals heterostructures with high accuracy rotational alignment. *Nano Lett.* **16**, 1989–1995 (2016).
35. Cao, Y. et al. Superlattice-induced insulating states and valley-protected orbits in twisted bilayer graphene. *Phys. Rev. Lett.* **117**, 116804 (2016).
36. Wang, L. et al. One-dimensional electrical contact to a two-dimensional material. *Science* **342**, 614–617 (2013).
37. Wong, D. et al. Cascade of electronic transitions in magic-angle twisted bilayer graphene. *Nature* **582**, 198–202 (2020).
38. Zondiner, U. et al. Cascade of phase transitions and Dirac revivals in magic-angle graphene. *Nature* **582**, 203–208 (2020).

Acknowledgements

We thank C. Dean, A. Young, J.-H. Chu, D. Cobden, S. Chen, X. Liu, P. Kim, B. Lian, A. MacDonald, L. Levitov and L. Fu for helpful discussions. Technical support for the dilution refrigerator was provided by A. Manna and Z. Fei. This work was primarily supported by NSF MRSEC grant no. 1719797. M.Y. acknowledges partial support from the Army Research Office under grant no. W911NF-20-1-0211. The theoretical calculation was partially supported by DOE BES grant no. DE-SC0018171. X.X. acknowledges support from the Boeing Distinguished Professorship in Physics. X.X. and M.Y. acknowledge support from the State of Washington funded Clean Energy Institute. This work made use of a dilution refrigerator system that was provided by NSF grant no. DMR-1725221. Y. Li acknowledges the support of the China Scholarship Council. K.W. and T.T. were supported by the Elemental Strategy Initiative conducted by the MEXT, Japan, and the CREST (JPMJCR15F3), JST.

Author contributions

M.Y., X.X. and M.H. conceived the experiment. M.H. and Y. Li fabricated the devices, assisted by Y. Liu. M.H. performed the measurements, with assistance from Y. Li and Y. Liu. J.C. performed band structure calculation. K.W. and T.T. provided the bulk BN crystals. M.H., X.X. and M.Y. analysed the data and wrote the paper with input from all authors.

Competing interests

The authors declare no competing interests.

Additional information

Extended data is available for this paper at https://doi.org/10.1038/s41567-020-1030-6.

Supplementary information is available for this paper at https://doi.org/10.1038/s41567-020-1030-6.

Correspondence and requests for materials should be addressed to X.X. or M.Y.

Reprints and permissions information is available at www.nature.com/reprints.

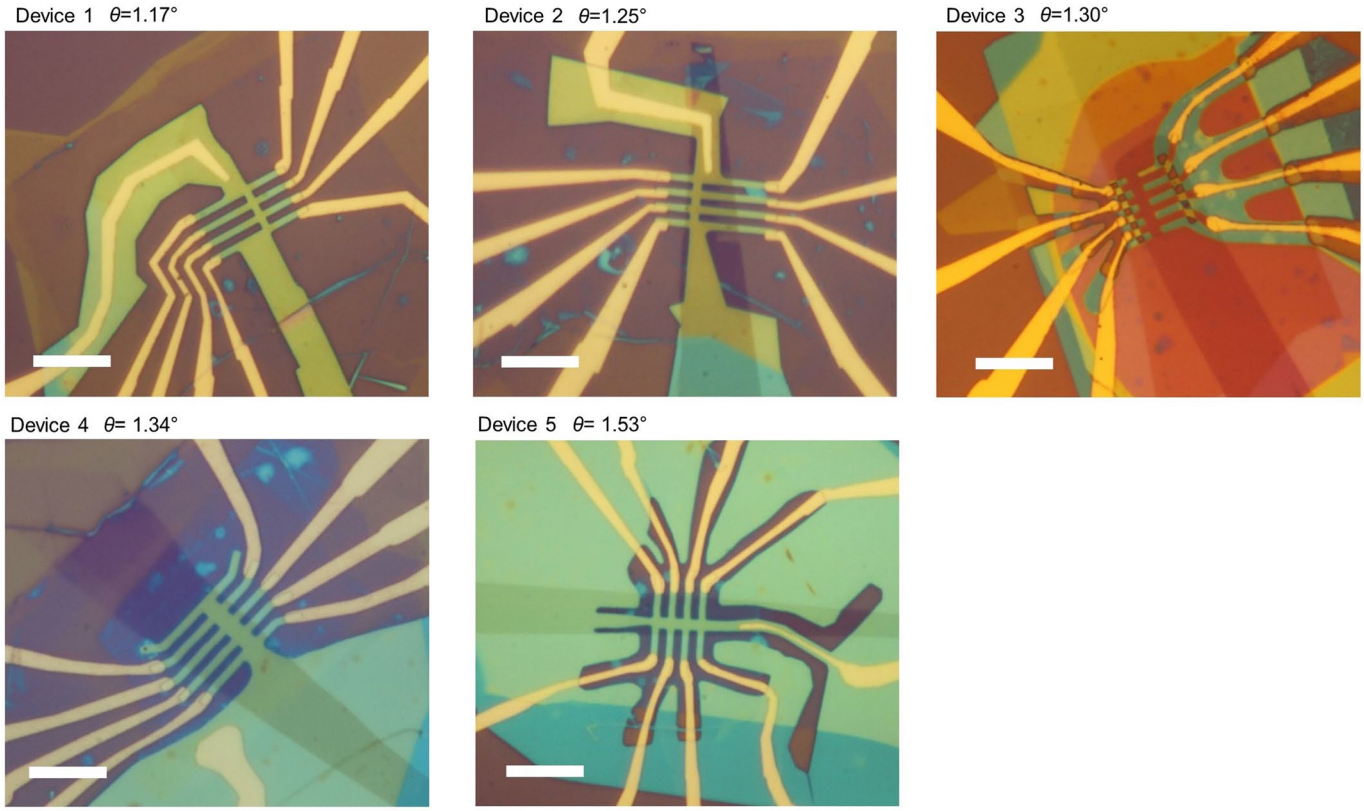

Extended Data Fig. 1 | Optical microscope images of the five tDBG devices. The twist angle of each device is denoted at the top left corner of each image. All scale bars are 10 μm.

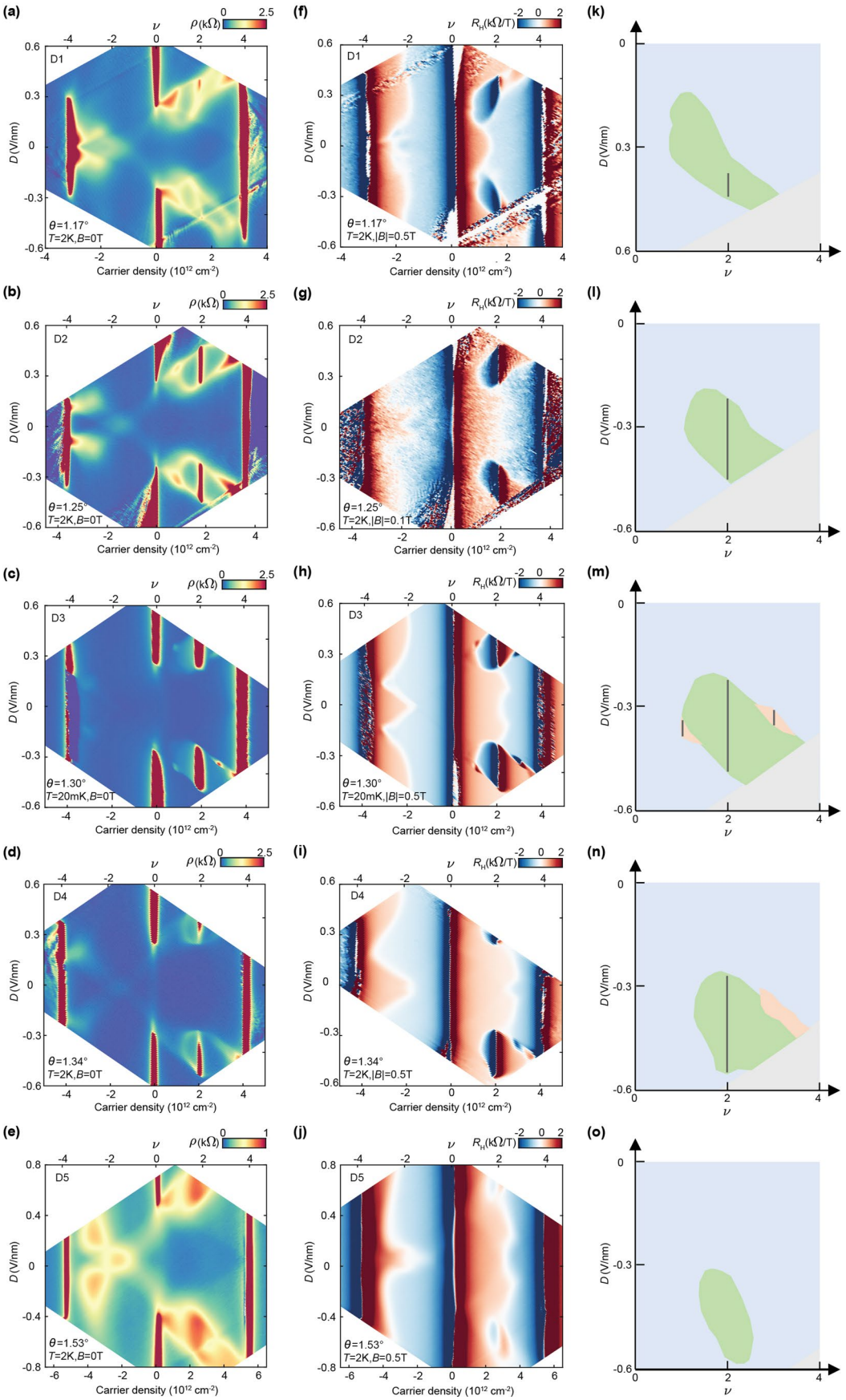

Extended Data Fig. 2 | See next page for caption.

Extended Data Fig. 2 | Transport in tDBG at a variety of twist angles. a-**e**, ρ as a function of n and D in all five devices acquired at $B = 0$ T. All are acquired at T = 2 K, except for **c** which is acquired at T = 20 mK. **f**-**j**, Corresponding R_H for the same devices. The maps in **f**, **h** and **i** are antisymmetrized at $|B| = 0.5$ T, the map in **g** is antisymmetrized at $|B| = 0.1$ T, and the map in **j** is acquired at $B = +0.5$ T but not antisymmetrized. **k**-**o**, Schematics of the phase diagram for each device. Blue corresponds to four-fold degeneracy, green corresponds to two-fold degeneracy, and orange indicates no remaining degeneracy. The dark gray lines denote CI states. The light gray coloring corresponds to experimentally inaccessible regions of the phase diagram.

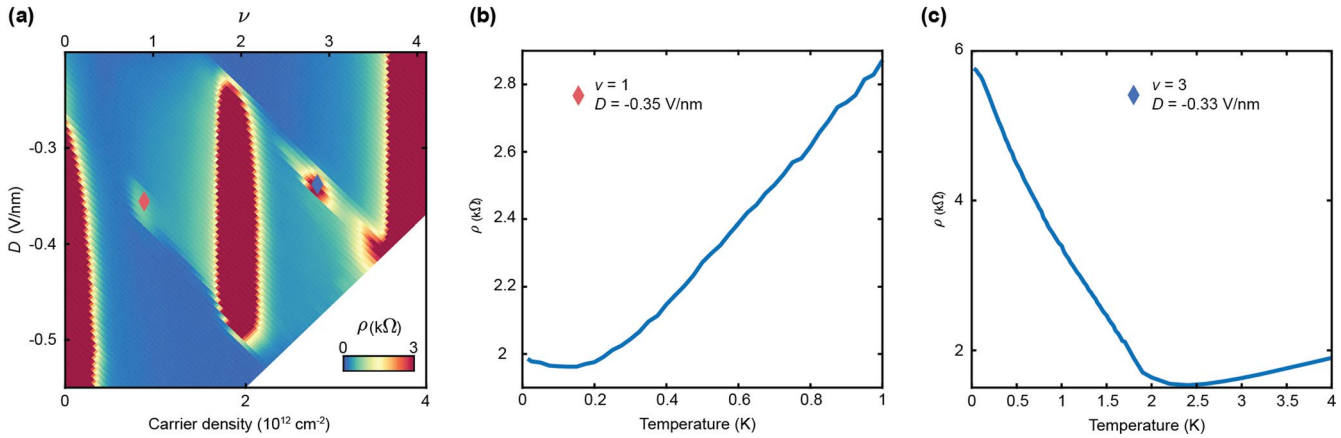

Extended Data Fig. 3 | Incipient CI states at $\nu = 1$ and 3 in device D3. a, ρ map surrounding the CI states in device D3 at T = 20 mK. **b**, ρ(T) acquired where the $\nu = 1$ CI state is most resistive. A weak metal-insulator transition is observed at T ≈ 150 mK. **c**, ρ(T) of the $\nu = 3$ CI state, exhibiting a metal-insulator transition at T ≈ 2.5 K.

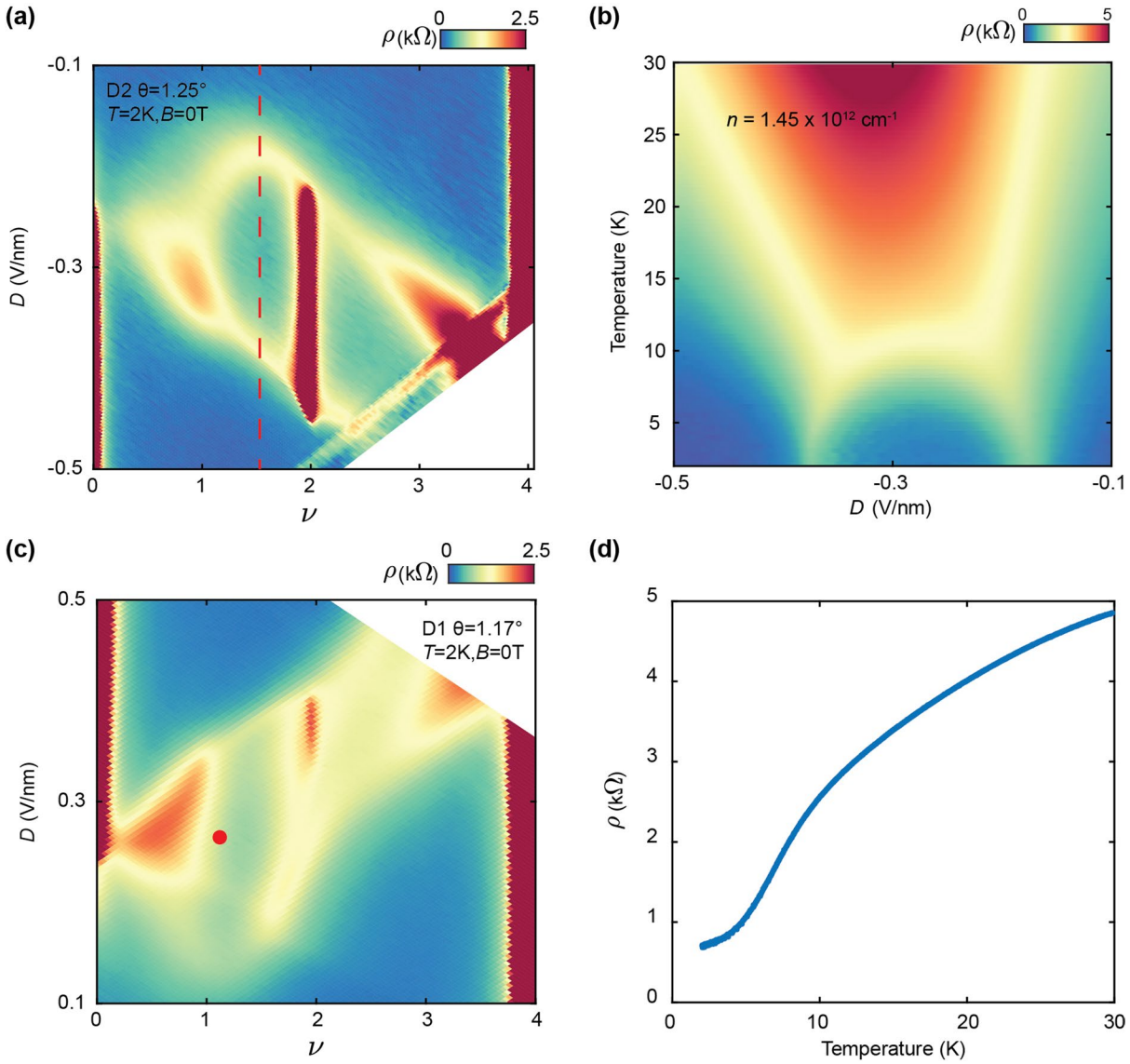

Extended Data Fig. 4 | Transport near the halo regions in devices D1 and D2. a, ρ map in device D2 at $T = 2$ K, exhibiting a CI state at $\nu = 2$ and a halo feature. **b**, ρ(T) as a function of D at fixed ν, acquired along the dashed red line in **a**. An arch-like feature is observed, similar to the behavior of device D3 shown in Fig. 2a. **c**, ρ map in device D1 at T = 2 K. A very weak CI state is observed at $\nu = 2$, as well as a distorted halo feature. **d**, ρ(T) acquired at the point marked by the red circle in **c**. Despite weaker correlations, an abrupt drop in ρ(T) is still observed to accompany the formation of the symmetry-broken halo region.

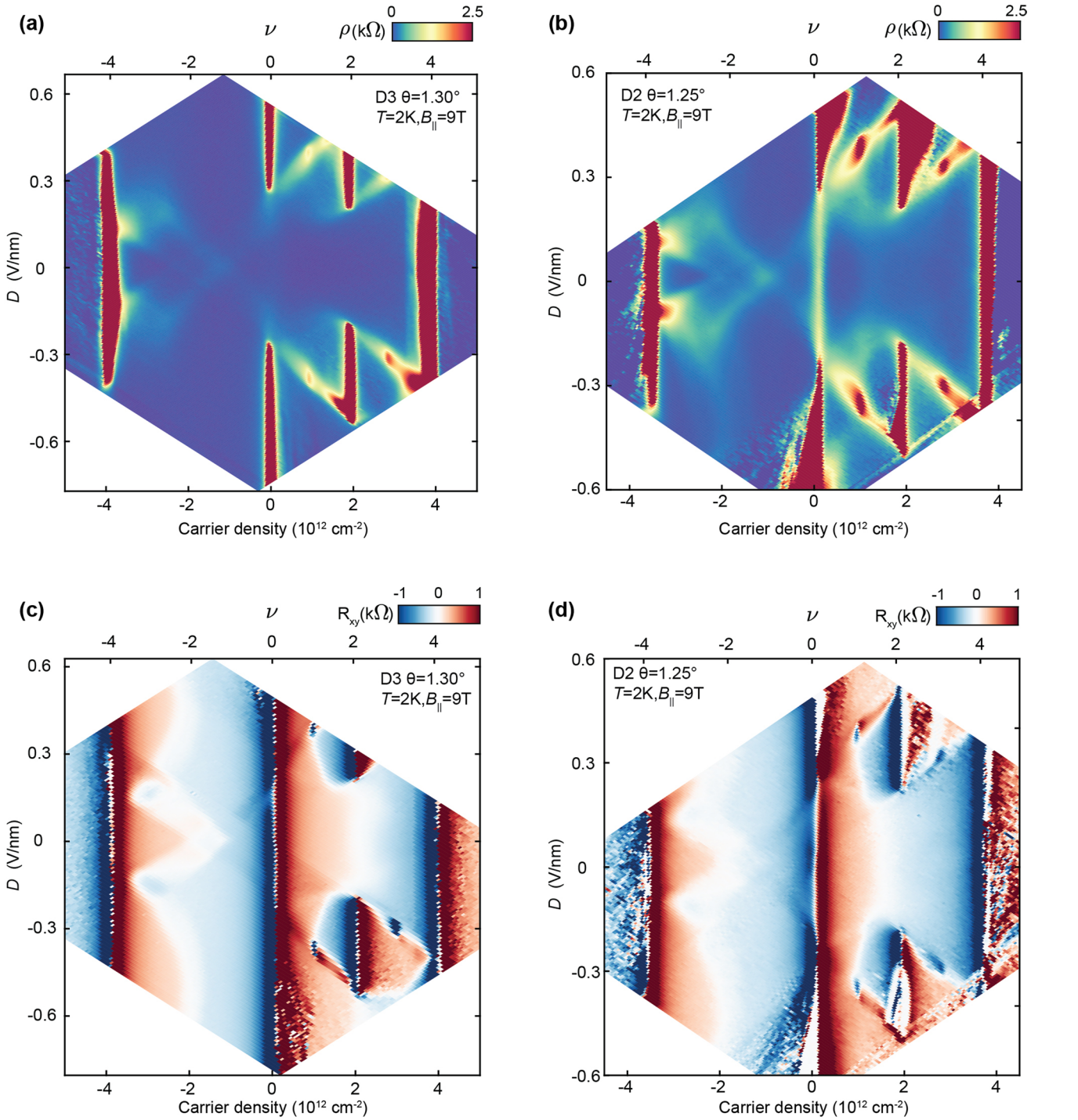

Extended Data Fig. 5 | Transport at $B_{||}$ = 9 T in devices D2 and D3. Maps of ρ at T = 2 K in devices **a**, D3 and **b**, D2, along with corresponding antisymmetrized Rxy in **c** and **d**. A small out-of-plane B component is also added in **b**-**d** in order to perform the (anti)-symmetrization.